



Time-integral iteration method for two-dimensional anomalous transport

J. E. Maggs  and G. J. Morales 

Department of Physics and Astronomy, University of California, Los Angeles, California 90025, USA



(Received 24 July 2022; accepted 12 September 2022; published 4 October 2022)

A methodology is developed to describe time-dependent phenomena associated with nonlocal transport in complex, two-dimensional geometries. It is an extension of the “iterative method” introduced previously to solve steady-state transport problems [Maggs and Morales, *Phys. Rev. E* **99**, 013307 (2019)], and it is based on the “jumping particle” concepts associated with the continuous-time random walk (CTRW) model. The method presented explicitly evaluates the time integral contained in the CTRW master equation. A modified version of the Mittag-Leffler function is used for the waiting-time probability distributions to incorporate memory effects. Calculations of the propagation of “anomalous transport waves” in various systems, with and without memory, illustrate the technique.

DOI: [10.1103/PhysRevE.106.045201](https://doi.org/10.1103/PhysRevE.106.045201)

I. INTRODUCTION

It is widely perceived that frontier investigations of transport phenomena of fundamental and practical interest require the consideration of nonlocal processes [1–7]. In the spatial domain, the nonlocality can arise from the presence of large fluctuations and/or ballistic effects that connect distant positions. In the time domain, nonlocality results from an effective memory associated with the intrinsic structure of the medium where transport occurs. In practice, spatial nonlocality and temporal memory are at work simultaneously, to varying degrees. In addition, most of the nonlocal transport environments are bounded, and often their characterizing parameters exhibit a zero-order nonuniformity. The present investigation considers a methodology for incorporating these essential features in nonlocal transport problems where a two-dimensional (2D) geometry is appropriate.

In this manuscript, the “jumping particle” iterative method for modeling steady-state nonlocal transport in bounded, nonuniform systems [8] is extended to include time dependence. The method for solving time-dependent problems is based upon the explicit, numerical evaluation of the time integrals contained in the master equation of the continuous-time random walk (CTRW) jumping particle model [9]. The jumping particle concept involves a waiting-time probability distribution function (PDF) and a jump distance PDF. The waiting-time PDF is time-dependent but is assumed to be independent of spatial location. A modified version of the one-parameter Mittag-Leffler function [10] is used to model a waiting-time PDF with memory of limited persistence. The jump distance PDF depends upon spatial location but is assumed independent of time. Two-parameter Lévy α -stable distributions are used to model the jump PDFs.

It should be noted that an extensive literature exists that describes nonlocal transport in terms of fractional derivatives [11–16]. Since this approach results from an asymptotic approximation to the underlying CRTW jumping particle

model, it is, in a certain sense, automatically included in the integral formulation being considered here. The scaling properties extracted from the fractional derivative formulation are reproduced by the numerical solutions of the time-integral, iterative method.

The manuscript is organized as follows. Section II presents the basis for the transport equation considered. Section III explains how the time integration is handled. A test of the methodology is provided for the 1D limit in Sec. IV. The properties of anomalous transport waves are illustrated in Sec. V. A discussion of the results and conclusions are found in Sec. VI. Appendix A explains the connection between the jumping particle formulation and Fick’s law.

II. TRANSPORT EQUATION

It is desired to compute the spatial profile resulting from nonlocal transport of some scalar quantity (e.g., density or temperature) in a 2D system. Transport is presumed to arise from “information carriers” (e.g., particles) that experience a transition or “jump” from one spatial location to another as described by the continuous-time random walk (CTRW) model [2]. The master equation describing the probability of a “particle” being at position (\bar{x}, \bar{y}) at time \bar{t} , $P(\bar{t}, \bar{x}, \bar{y})$, is

$$\begin{aligned}
 P(\bar{t}, \bar{x}, \bar{y}) &= \delta(\bar{x})\delta(\bar{y}) \left\{ 1 - \int_0^{\bar{t}} \psi(\bar{t}') d\bar{t}' \right\} + \int_0^{\bar{t}} d\bar{t}' \psi(\bar{t} - \bar{t}') \\
 &\times \int_{-\infty}^{\infty} \int_{-\infty}^{\infty} d\bar{x}' d\bar{y}' \eta(p(\bar{x}', \bar{y}'), \bar{x} - \bar{x}', \bar{y} - \bar{y}') P(\bar{t}', \bar{x}', \bar{y}').
 \end{aligned} \tag{1}$$

The quantities \bar{t} , \bar{x} , \bar{y} are time and spatial position measured in physical units. The quantity $P(\bar{t}, \bar{x}, \bar{y})$ is a joint probability distribution function in the CTRW model, with a δ -function initial condition, $P(\bar{t} = 0, \bar{x}, \bar{y}) = \delta(\bar{x})\delta(\bar{y})$.

The waiting-time probability, the probability of a particle not jumping in the time interval $[0, \bar{t}]$, is $\psi(\bar{t})d\bar{t}$ and the probability of a particle jumping from (\bar{x}', \bar{y}') to (\bar{x}, \bar{y}) is $\eta(p(\bar{x}, \bar{y}), \bar{x} - \bar{x}', \bar{y} - \bar{y}')d\bar{x}'d\bar{y}'$. In this study, the waiting-time probability distribution function, $\psi(\bar{t})$, is assumed to be independent of position, and the jump probability distribution function, $\eta(p(\bar{x}, \bar{y}), \bar{x}, \bar{y})$, is assumed to be independent of time. The parameters characterizing the jump distribution are allowed to vary with position, and the function $p(\bar{x}, \bar{y})$ specifies the parameter variation. The initial condition is taken to be that all the particles are located at $(\bar{x}, \bar{y}) = 0$.

The ability to choose the functional form of the waiting-time probability distribution function allows for studying a variety of temporal evolutions (e.g., memory effects) that result in subdiffusive dynamics. Here the waiting-time probability distribution function (PDF) is taken to be proportional to the single-parameter Mittag-Leffler function defined as

$$E_a(-(\bar{t}/\bar{\tau})^a) = \sum_{k=0}^{\infty} \frac{(-(\bar{t}/\bar{\tau})^a)^k}{\Gamma(1 + ak)}, \quad 0 < a \leq 1. \quad (2)$$

The time variable ranges from 0 to $t_{\text{up}} = \bar{t}_{\text{up}}/\bar{\tau}$, where \bar{t}_{up} denotes the upper limit, in physical units, of the time interval considered in numerical calculations. The parameter $\bar{\tau}$ is referred to as the ‘‘characteristic waiting time’’ of the waiting-time PDF. Setting the parameter a in Eq. (2) equal to unity ($a = 1$) results in a waiting-time PDF that is the Poisson distribution. The Poisson distribution is the exponential function and represents a Markovian process in which memory effects are absent. The Mittag-Leffler PDF with parameter values between 0 and 1 ($0 < a < 1$) represents processes with memory, as the asymptotic form of the Mittag-Leffler function exhibits an algebraic tail and scales as $E_a(-\bar{t}^a) \sim 1/\bar{t}^a$. Probability distribution functions are normalized so that the integral of the function over time is unity. Since the ‘‘tail’’ of the Mittag-Leffler function does not decay rapidly, it is necessary to use some technique to truncate the slowly decaying tail to obtain a finite result for the normalizing integral. Truncation is accomplished here by limiting the length of the slowly decaying tail to $\bar{t} \leq \bar{t}_{\text{lim}}$. For $\bar{t} > \bar{t}_{\text{lim}}$, the Mittag-Leffler function is modified to decay as $\exp(-(\bar{t} - \bar{t}_{\text{lim}}))$. If \bar{t} is everywhere less than \bar{t}_{lim} (i.e., $\bar{t}_{\text{lim}} \geq \bar{t}$), then the tail is limited by using ‘‘top-hat’’ truncation in the time dimension over the range $0 \leq \bar{t} \leq \bar{t}_{\text{up}}$. There is no need to modify the Mittag-Leffler function when $a = 1$ because it is already exponentially decaying. The time interval over which a modified Mittag-Leffler PDF represents a memory effect is determined by the value of the parameter, \bar{t}_{lim} . Therefore, the parameter \bar{t}_{lim} is referred to, in the following discussion, as the memory persistence time.

If the parameter a is between 0 and 1, $0 < a < 1$, the modified Mittag-Leffler function, \tilde{E}_a , has the integral representation [17]

$$\left\{ \begin{aligned} \tilde{E}_a(-(\bar{t}/\bar{\tau})^a) &= \int_0^{\infty} dx \frac{e^{-x\bar{t}}}{\pi} \frac{x^{(a-1)} \sin(\pi a)}{x^{2a} + 2x^a \cos(\pi a) + 1} \Bigg\}; \quad \left[\frac{\bar{t}}{\bar{\tau}} \leq \frac{\bar{t}_{\text{lim}}}{\bar{\tau}} \right], \\ \tilde{E}_a(0) &= 1; \quad 0 < a < 1 \end{aligned} \right. \quad (3)$$

$$\tilde{E}_a(-(\bar{t}/\bar{\tau})^a) = \tilde{E}_a(-(\bar{t}_{\text{lim}}/\bar{\tau})^a) \exp\left(-\left(\frac{\bar{t}}{\bar{\tau}} - \frac{\bar{t}_{\text{lim}}}{\bar{\tau}}\right)\right); \quad \left[\frac{\bar{t}}{\bar{\tau}} > \frac{\bar{t}_{\text{lim}}}{\bar{\tau}} \right].$$

The integral representation of the Mittag-Leffler function given in Eq. (3) is useful to obtain a numerical evaluation of the function when $0 < a < 1$. To ensure that the modified Mittag-Leffler function represents a PDF, it is normalized so that its integral is unity over the interval sampled,

$$\tilde{E}_a \rightarrow \tilde{E}_a / \int_0^{t_{\text{up}}} dt' \tilde{E}_a(t'). \quad (4)$$

In lieu of using a Laplace transform approach and obtaining fractional temporal derivative operators [18], this study presents solutions of the transport equation based upon the explicit numerical evaluation of the time integrals in Eq. (1) using $\psi = \tilde{E}_a$.

Solutions to Eq. (1) are numerically computed at discrete spatial points, (\bar{x}_i, \bar{y}_j) . In a discrete space, it is convenient to introduce an expression for the transported scalar, $T(\bar{t}, \bar{x}, \bar{y})$, in terms of individual probabilities $T(\bar{t}, \bar{x}, \bar{y}) = \sum_i \sum_j A_{i,j} P_{i,j}(\bar{t}, \bar{x}, \bar{y})$, where each $P_{i,j}(\bar{t}, \bar{x}, \bar{y})$ satisfies Eq. (1) with the following initial condition: $P_{i,j}(0, \bar{x}, \bar{y}) = \delta(\bar{x} - \bar{x}_i)\delta(\bar{y} - \bar{y}_j)$. The use of the variable name T for the generic scalar is motivated by applications in which it represents the temperature of a bounded system. From the definition of the scalar T , the transport equation for $T(\bar{t}, \bar{x}, \bar{y})$ is obtained from Eq. (1),

$$\begin{aligned} T(\bar{t}, \bar{x}, \bar{y}) &= T(0, \bar{x}, \bar{y})I_{\psi}(\bar{t}) + S(\bar{t}, \bar{x}, \bar{y}) + \int_0^{\bar{t}} ds \psi(t-s) \\ &\quad \times \iint_{-\infty}^{\infty} d\bar{x}'d\bar{y}' \eta(p(\bar{x}', \bar{y}'), \bar{x} - \bar{x}', \bar{y} - \bar{y}') T(s, \bar{x}', \bar{y}'). \end{aligned} \quad (5)$$

The term $S(\bar{t}, \bar{x}, \bar{y})$ in Eq. (5) has been added to represent the contribution from external sources and $I_{\psi}(\bar{t}) = 1 - \int_0^{\bar{t}} ds \psi(s)$. The term $T(0, \bar{x}, \bar{y})I_{\psi}(\bar{t})$ represents the system response to the initial conditions. The term $I_{\psi}(\bar{t})$ decays with time, and the rate of decay depends upon the parameters chosen for the Mittag-Leffler function. For example, with a Poisson waiting-time distribution ($a = 1$), $I_{\psi}(\bar{t}) = e^{-\bar{t}}$.

For practical applications, it is useful to have equations that describe systems of limited physical extent. For this purpose, it is assumed that the jump distributions, η , are nonzero only over a limited spatial region, R . Further, assume that the extent of the region R is characterized by a scale length, \bar{L} , and that all points in the region have magnitudes less than \bar{L} , $\{|\bar{x}|, |\bar{y}| \leq \bar{L}\}$. The jump distributions are required to have zero value outside the spatial region R . The ‘‘truncation’’ of the jump distributions is accomplished by multiplying them by a ‘‘top-hat’’ function,

$$F_{\text{th}}(\bar{x}, \bar{y}) = \begin{cases} 1, & (\bar{x}, \bar{y}) \in R, \\ 0, & (\bar{x}, \bar{y}) \notin R. \end{cases} \quad (6)$$

Consider the truncation of the jump distribution with peak located at the point (\bar{x}, \bar{y}) , $\eta(p(\bar{x}, \bar{y}), \bar{x} - \bar{x}', \bar{y} - \bar{y}')$. Since the jump distributions are probability densities, it is

required that

$$\begin{aligned} & \int_{-\infty}^{\infty} d\bar{y}' \int_{-\infty}^{\infty} d\bar{x}' \eta(p(\bar{x}, \bar{y}), \bar{x} - \bar{x}', \bar{y} - \bar{y}') F_{\text{th}}(\bar{x}', \bar{y}') \\ &= \oint\!\!\!\oint_R d\bar{x}' d\bar{y}' \eta(p(\bar{x}, \bar{y}), \bar{x} - \bar{x}', \bar{y} - \bar{y}') \\ &= 1; \forall (\bar{x}, \bar{y}) \in R. \end{aligned} \quad (7)$$

Normalizing the position variables to \bar{L} and the time to $\bar{\tau}$ gives dimensionless spatial coordinates $(x, y) = (\bar{x}/\bar{L}, \bar{y}/\bar{L})$, and dimensionless time, $t = \bar{t}/\bar{\tau}$. For convenience in numerical calculation of the spatial integral, change the notation to a double integral and set T , the temperature, to zero for points outside the region R , $T(t, x, y) = 0$, $(x, y) \notin R$. The condition that the temperature is zero outside the region R is a boundary condition for the system. In the scaled coordinates, the model transport equation for $T(t, x, y)$ is

$$\begin{aligned} & T(t, x, y) \\ &= \int_0^t ds \psi(t-s) \int_0^1 \int_0^1 dx' dy' \eta'(p(x', y'), x-x', y-y') \\ & \quad \times T(s, x', y') + T_0(x, y) I_\psi(t) + S(t, x, y); T(t, x, y) \\ &= 0, \quad (x, y) \notin R. \end{aligned} \quad (8)$$

In Eq. (8), the dimensionless jump distribution is denoted by $\eta' = \eta \bar{L}^2$, and $T_0(x, y)$ is a term used to set the initial value of the temperature profile.

The jump distribution functions are chosen to be Lévy α -stable distributions as discussed in Maggs and Morales [8]. The Lévy α -stable distributions are characterized by two parameters, (α, γ) . The order of the distribution, α , is restricted to the range $1 \leq \alpha \leq 2$, and the width of the distribution, γ , is positive ($\gamma > 0$). Lévy distributions are computed numerically using an inverse Fourier transform of the characteristic function, $\tilde{\mathcal{L}}(\alpha, \gamma, k_F)$, with k_F denoting the Fourier wave number. An example of the characteristic function suitable for describing an isotropic jump distribution in 2D geometry with (x, y) coordinates is

$$\ln[\tilde{\mathcal{L}}(\alpha, \gamma, k_F)] = -(\gamma |k_F|)^\alpha, \quad |k_F| = (k_x^2 + k_y^2)^{\frac{1}{2}}. \quad (9)$$

The parameters (α, γ) are allowed to be functions of position, in which case the jump distributions are separately computed at each spatial point in the domain using the values of (α, γ) at that point. The characteristic function of an anisotropic form of the Lévy distribution, suitable for describing transport in magnetic confinement devices, is given in [21]. Finding specific values of the parameters, $[\alpha, \gamma, \bar{\tau}]$, needed to apply the transport model to a physical system depends upon experimental measurements of the system to be modeled. An example of the methods used to select parameter values for modeling the steady-state temperature profile in the LHD helical plasma device is given in [21].

The model transport system confined to the spatial region, R , is taken to consist of a contiguous spatial region R_{tr} , in which transport is nonlocal, surrounded by a heat reservoir region, R_{hr} , $R_{\text{tr}} + R_{\text{hr}} = R$. The interface between the regions R_{tr} and R_{hr} is treated in the following fashion. Jumps are allowed from the transport region R_{tr} into the heat reservoir region R_{hr} , but not from R_{hr} into the region R_{tr} . The jump

distributions in region R_{tr} are set to zero outside the region R by using “top-hat” truncation as described by Eq. (6). The truncated jump distributions are renormalized, as described by Eq. (7), so that their spatial integrals are unity as befits a probability distribution. The temperature of the heat reservoir region, R_{hr} , is maintained at zero so that particles jumping from R_{tr} into R_{hr} transport energy out of R_{tr} , and thus represent an energy loss process for the transport region.

The discrete form of Eq. (8) is obtained by using a calculation grid of $(N_t + 1) \times (N + 1) \times (N + 1)$, with separate points to represent the scalar variable, $T(t, x, y)$. The grid representing the spatial part of $T(t, x, y)$ has $(N + 1) \times (N + 1)$ evenly spaced points, with spacing h , $(x_i = ih, y_j = jh)$ and $0 \leq i \leq N; 0 \leq j \leq N$. The vector representing time has $(N_t + 1)$ evenly spaced points with spacing Δt , $t_m = m\Delta t$, and $0 \leq m \leq N_t$. The discrete form of Eq. (8) is then given as

$$\begin{aligned} & T(m, i, j) = I_\psi(m) T_0(i, j) + S(m, i, j) \\ & \quad + \left[\sum_{k=0}^m \Delta t \psi(m, k) \right. \\ & \quad \left. \times \left\{ \sum_{l=0}^N \sum_{n=0}^N h^2 \eta'_{\text{SA}}(i, l, n, j) T(k, l, n) \right\} \right]. \end{aligned} \quad (10)$$

In Eq. (10), the symbol, $[\Sigma]$, indicates that the sum over the time index k is to be interpreted as a symbolic representation of a numerical approximation to the time integral. The sizes of the temporal and spatial grids are determined by the physical phenomena under study. For spatial grids, a grid size small enough to properly model the transport coefficients is needed. Transport coefficients are proportional to γ^α , with γ the width of the jump distributions. The size of the spacing in the spatial grid, h , must be small enough that $\gamma \geq h$ to get an accurate representation of the jump distributions. The size of the temporal grid must be large enough to encompass the time intervals of the physical processes under study. The time step is always greater than or equal to $\bar{\tau}$, the characteristic time of the waiting-time distribution. Temporal phenomena with timescales less than $\bar{\tau}$ are not represented in the jumping particle model.

The self-adjoint form of the jump probability distribution function is represented by the term η'_{SA} in Eq. (10). It is crucial for obtaining correct solutions, when the parameters are allowed to have spatial gradients, that the self-adjoint (SA) form of the jump distribution is used. The self-adjoint form is obtained by ensuring that η'_{SA} remains unchanged under interchange of i with l (x with x') and j with n (y with y'),

$$\eta'_{\text{SA}}(i, l, n, j) = [\eta'(i, l, n, j) + \eta'(l, i, j, n)]/2. \quad (11)$$

III. TIME INTEGRATION

The time integral term in Eq. (10) can be recast as

$$\begin{aligned} & \left[\sum_{k=0}^m \Delta t \psi(m, k) \left\{ \sum_{l=0}^N \sum_{n=0}^N h^2 \eta'_{\text{SA}}(i, l, n, j) T(k, l, n) \right\} \right] \\ &= \left[\sum_{k=0}^m \Delta t \psi(m, k) T_{\text{si}}(k, :, :), \right. \end{aligned} \quad (12)$$

with the spatial iteration term (denoted by subscript “si”) given by

$$T_{\text{si}}(k, :, :) = \sum_{l=0}^N \sum_{n=0}^N h^2 \eta'_{\text{SA}}(:, l, n, :) T(k, l, n). \quad (13)$$

The process for finding solutions using Eq. (12) is as follows. An initial profile in space and time is chosen. Starting from that profile, an updated spatial profile at each time step is computed. The updated profile at time step k , $T_{\text{next}}(k, :, :)$, is computed from the old profile at time step k , $T_{\text{prev}}(k, :, :)$. The updated profile is initially zero and is computed from the previous profile by adding up all the contributions from jumping particles originating at each point in R_{tr} . That is, $T_{\text{next}}(k, :, :) = T_{\text{prev}}(k, i, m) \eta'_{\text{SA}}(i, :, :, m) + T_{\text{next}}(k, :, :)$ for all points (i, m) in R_{tr} . After the jumps from all the points in R_{tr} are added up, the temperature in the heat reservoir region, R_{hr} , is set to zero. This process is repeated for all time steps and then the time integral portion of Eq. (12) is computed. The process is repeated using the updated space-time profile as the beginning profile for the next iteration, until the changes in the space-time profile, after iteration, are below a specified limit.

The reader is reminded that the notation $[\Sigma$, involving the sum over k in Eq. (12) represents a method for performing the numerical integration rather than an actual straightforward summation. In numerical computations, the spatial iteration term is evaluated at fixed, evenly spaced time points of the normalized time variable $t(k) = k \Delta t = k$. That is, the value of Δt is 1 ($\Delta t = 1$), so that the physical time points are spaced at intervals of $\bar{\tau}$. To speed computation, spatial profiles are computed only at integer values of normalized time. This restriction limits the method to physical processes that occur on timescales longer than the characteristic waiting time.

Computing spatial profiles at integer values of normalized time means the discrete time step in numerical calculations is the characteristic waiting time $\bar{\tau}$. The accuracy of a numerical evaluation of the time integral is improved by employing the subsampling technique. In subsampling, the temporal resolution is increased by a factor sr , referred to as the “sampling rate.” The new time variable becomes $t_1 = t(0) : \frac{1}{\text{sr}} : t(N_t)$ and has $N_{\text{sr}} + 1$ points, $N_{\text{sr}} = \text{sr}N_t$. The higher resolution waiting-time PDF becomes $\psi(m_1, k_1)$ with both m_1 and $k_1 \in [0, \text{sr} \times N_t]$ and $\Delta t_1 = \Delta t/\text{sr}$. Using Simpson’s rule with a sampling rate of $\text{sr} = 2$, or Boole’s rule with a sampling rate of $\text{sr} = 4$, not only provides the advantage of improved accuracy, but ensures that every interval of the original time variable becomes an interval with the proper number of points for applying the integration formulas (i.e., an odd number for both methods). With $\text{sr} = 2$, $\Delta t \rightarrow \Delta t/2 = \Delta t_1$ and the interval from t to $t + \Delta t$ then has three points, $t, t + \Delta t_1, t + 2\Delta t_1$, and Simpson’s rule can be applied to every interval of the original time variable. Similarly, with $\text{sr} = 4$, $\Delta t \rightarrow \Delta t/4 = \Delta t_1$ and the interval from t to $t + \Delta t$ then has five points, $t, t + \Delta t_1, t + 2\Delta t_1, t + 3\Delta t_1, t + 4\Delta t_1$, and Boole’s rule can be applied to find the value of the time integral at every integer value of normalized time. The subsampling technique means that there is no *a priori* requirement on the length of the

original time variable in implementing a suitable integration algorithm.

In the underlying nonlocal transport scheme, the spatial profiles are computed iteratively and, at each step in the iteration process, spatial profiles are calculated only at integer values of normalized time. With the increased temporal resolution associated with the subsampling technique used to compute the time integral, the spatial iteration term is required at each subsampled time step. To decrease computation time, linearly interpolated spatial profiles are used for time points between integer values of the subsampled time variable. Consider the spatial portion of the iteration profile at time points k_1 of the subsampled time variable, $T_{\text{si}}^1(k_1, :, :)$. For the points k_1 that correspond to integer values of the original time variable, the values of the spatial iteration term at those points can be used without alteration. For points k_1 that are between intervals of the original time vector, the value of the spatial term at time point k_1 is estimated using linear interpolation. For example, using Simpson’s rule, with $\text{sr} = 2$, the profile at $k_1 = k + 1/2$ is

$$T_{\text{si}}^1(k_1 = k + \frac{1}{2}, :, :) = \frac{1}{2}[T_{\text{si}}(k + 1, :, :) + T_{\text{si}}(k, :, :)]. \quad (14)$$

The interpolated spatial profile is then used at step k_1 in the computation of the time integral. Analogous linear interpolation of spatial profiles is used when applying Boole’s rule. This process results in a profile with $\text{sr} \times N_t + 1$ time points computed from only $N_t + 1$ spatial profiles. Time integration is performed using spatially interpolated profiles with Simpson’s rule if $\text{sr} = 2$ or with Boole’s rule if $\text{sr} = 4$. The final output of the procedure is profiles computed at integer values of the original normalized time variable. The subsampling technique increases computation time by a factor of sr , so the smallest value of sr that yields sufficient accuracy should be used.

From a detailed comparison (not shown) of the application of Simpson’s rule, and of Boole’s rule to the solution of a known analytic 2D transport problem, it has been found that both methods yield nearly identical results. Since computation times are longest for Boole’s rule, the simpler Simpson’s rule is chosen as the preferred method. In all subsequent computations reported here, Simpson’s rule is used for time integration.

IV. ANOMALOUS TRANSPORT IN 1D

The ability of the time-dependent jumping particle model to represent various anomalous transport phenomena is demonstrated by considering transport in the simpler limit of one spatial dimension. The 1D version of Eq. (10) is

$$T(m, i) = T_0(i)I_\psi(m) + S(m, i) + \left[\sum_{k=0}^m \Delta t \psi(m, k) \left\{ \sum_{l=0}^N h \eta'_{\text{SA}}(i, l) T(k, l) \right\} \right]. \quad (15)$$

Equation (15) is solved next with various values of model parameters to elucidate the transport phenomena represented by the model. The results of numerical computations

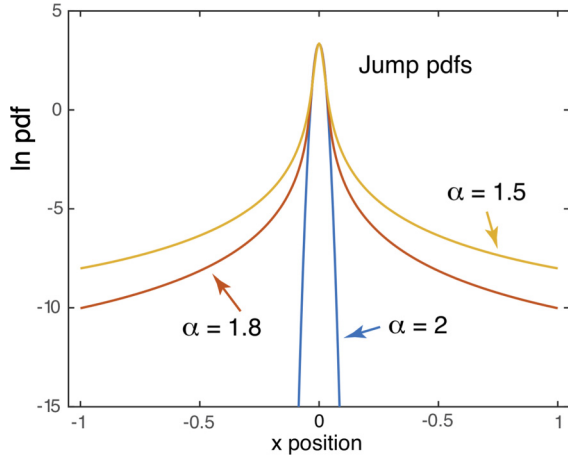


FIG. 1. The natural logarithm of Lévy-stable probability distribution for three values of α as indicated. All distributions have the same width $\gamma = 2h$.

are compared to a well-known 1D problem, namely the temporal evolution of a δ -function pulse at $t = 0, x = 0$ under a standard diffusive process (Fick’s law) with constant diffusion coefficient D_c . The diffusion equation and the analytic solution, $T_A(t, x)$, for this case are

$$\frac{\partial T(t, x)}{\partial t} = D_c \frac{\partial^2 T(t, x)}{\partial x^2} + \delta(t)\delta(x),$$

$$T_A(t, x) = \frac{1}{2\sqrt{\pi D_c t}} \exp\left(-\frac{x^2}{4D_c t}\right). \quad (16)$$

In Eq. (16) dimensionless variables are used, and the dimensionless diffusion coefficient D_c is related to the physical diffusion coefficient, \bar{D}_c , as $D_c = \bar{D}_c \bar{\tau}/L^2$. In the jumping particle model, the standard diffusion situation is represented by the parameter set, $[\alpha = 2, a = 1]$. The extent to which this limiting parameter set and the jumping particle model represent standard diffusion is discussed in detail in Appendix A. The salient finding is that the jumping particle model equation with $[\alpha = 2, a = 1]$ becomes the diffusion equation at long times when the average jump length becomes small compared to the effective scale length of the evolving profile.

A. Superdiffusion

The dynamics of particles in space are determined by the “jump” probability distribution function. The jump PDFs used in this study are proportional to two-parameter Lévy α -stable distributions, $\eta(\alpha, \gamma, x)$, characterized by the parameters $[\alpha, \gamma]$. The characteristic function (Fourier transform) of the 1D Lévy α -stable distribution is proportional to $\exp(-|\gamma k|^\alpha)$. Asymptotically, for values of α less than 2, $1 \leq \alpha < 2$, the Lévy distribution decays as $\sim 1/|x|^{1+\alpha}$, so the parameter α determines how fast the tails of the distribution decay. The parameter γ determines the width of the distribution. Figure 1 shows the natural logarithm of the jump probability distribution for three values of α . All distributions shown in Fig. 1 have the same width, $\gamma = 2h$, where h is the spacing of points on the spatial calculation grid. For $\alpha = 2$, the Lévy distribution is a Maxwellian, and the width parameter γ is related to the standard deviation σ as $\gamma = \sqrt{2} \sigma$.

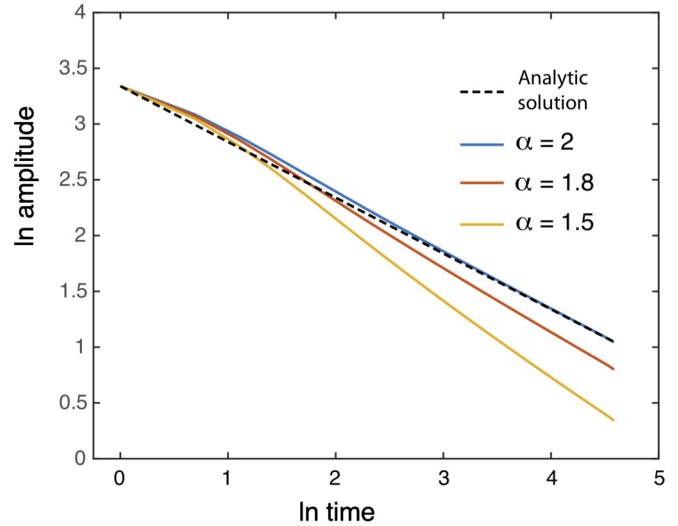


FIG. 2. The temporal decay of the peak of an initial profile of Gaussian shape, $T_A(1, x)$, is compared to the analytic solution for standard diffusion (dashed curve) and three values of α (as indicated). α values less than 2 are associated with the phenomenon of superdiffusion.

To compare transport for different values of α , the temporal decay of the analytic solution at $t = 1, T(0, x) = T_A(1, x) = \exp(-x^2/4D_c)/2\sqrt{\pi D_c}$, is computed using the three jump distributions shown in Fig. 1. The width of all distributions is $\gamma = 2h$, two grid spacings, so that $\gamma^2 = 4h^2 = D_c$. The natural logarithms of the numerically computed profiles at the value $x = 0$ versus the natural logarithm of time are shown in Fig. 2. The blue trace shown in Fig. 2 is the standard diffusion case ($[\alpha = 2, a = 1]$), and, as discussed in Appendix A, the jumping particle model solution initially departs from the analytic solution (dashed black line) due to higher-order spatial derivatives contained in the jumping particle model, but at long times it agrees with the analytic solution. All numerical solutions have an initial transient in which profile spreading is slower than the analytic solution. The numerically computed profile amplitude decays (asymptotically) at the same rate as the analytic solution for $\alpha = 2$ and at faster rates for the other two values of α . The smaller the value of α , the faster the profile decays. Transport at rates faster than the standard rate of diffusion (here represented by the analytic solution) is referred to as “superdiffusion.”

Figure 3 shows the spatial profiles at $t = 100$ for the cases shown in Fig. 2. The spatial spreading of the profiles increases for decreasing value of α . The spatial integral of the temperature profile can be thought of as a measure of energy content. The spatial integrals are constant in time until the time that the profile contacts the boundary. By “contacts” it is meant that the boundary causes a noticeable change in the profile derivative near the boundary. Once the profile contacts the boundary, the value of the spatial integral decreases because energy is lost to the boundary region. In the examples shown in Fig. 3, only the $\alpha = 1.5$ case contacts the boundary over the time interval used for this calculation. Note that the analytic spatial profile (black dashed line) and the $\alpha = 2$ profile (solid blue line) agree quite well at this late time.

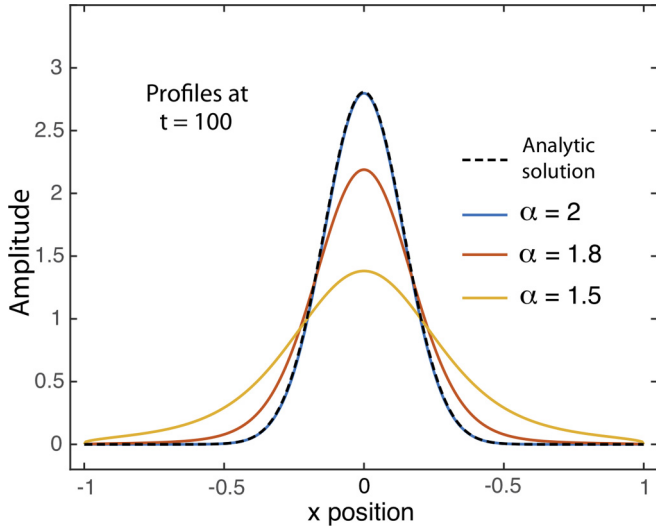


FIG. 3. The spatial profiles for the standard diffusion analytic solution (dashed curve) and three values of α (as indicated) are shown for a scaled time $t = 100$. Profile spreading is strongest for the smallest value of α (yellow trace).

B. Subdiffusion

The time dynamics of jumping particles is determined by the functional form of the waiting-time probability distribution function. In this study, the waiting-time PDF has the functional form of the modified Mittag-Leffler function given in Eq. (3). Figure 4 compares four possible waiting-time distributions. Three are associated with examples of the modified Mittag-Leffler function in which memory is present, and the other is associated with the Poisson distribution indicated by the label “No memory.” The three examples of PDFs with memory all have the parameter $a = 0.9$. They are distinguished by the persistence of the memory, $t_{lim} =$

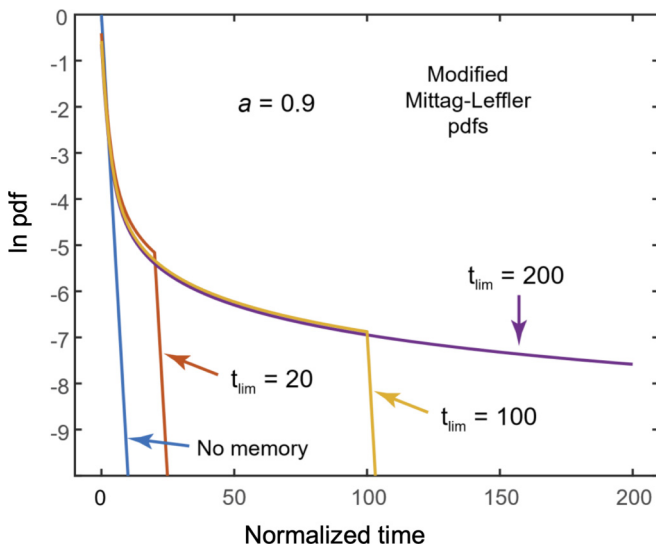


FIG. 4. The natural logarithm of the PDFs associated with the modified Mittag-Leffler function is shown for $a = 0.9$ and three values of the memory limit parameter, t_{lim} . Also shown for comparison is the PDF with no memory (blue trace).

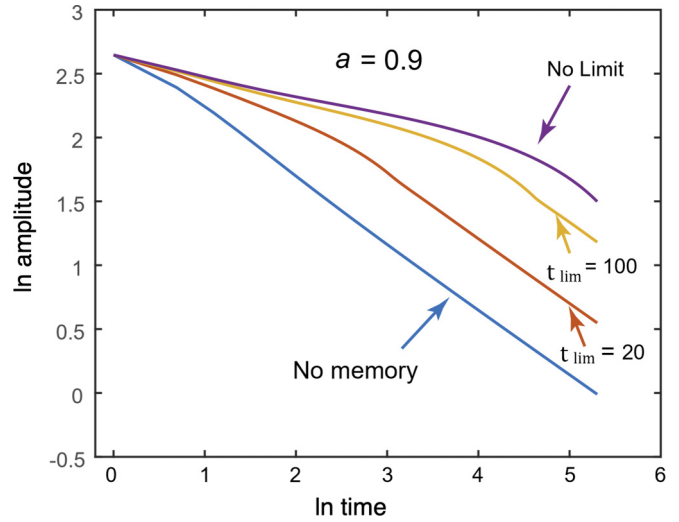


FIG. 5. Memory and memory persistence affect the rate of temporal decay of an initial Gaussian spatial profile for $\alpha = 2$. The case labeled “No Limit” has $t_{lim} = 200 = t_{up}$. Compare this figure to Fig. 2.

20, 100, 200. The case with $t_{lim} = 200$ is an example of a persistent memory, or the “no limit” case, because the length of the time interval considered in subsequent numerical calculations is $t_{up} = 200$.

To illuminate the effects of various waiting-time distributions and compare results to cases of superdiffusion, the temporal decay of the initial Gaussian profile $T_A(1, x)$ is computed for the waiting-time probability distributions shown in Fig. 4. The jump distributions for all cases are Lévy distributions with $\alpha = 2$, so that superdiffusion is not present. The case with $a = 1$ corresponds to a Poisson waiting-time distribution so that this case is the same as the $\alpha = 2$ case shown in Fig. 2. Solutions for this set of parameters [$\alpha = 2, a = 1$] are labeled as “No memory” in the figures.

Figure 5 shows the temporal decay of the initial spatial Gaussian profile, $T_A(1, x)$, for the “No memory” case and for three cases corresponding to the modified Mittag-Leffler PDFs shown in Fig. 4. All cases with memory decay at a slower rate than for the “No memory” case. This type of behavior is referred to as “subdiffusive” behavior. The case with persistent memory (the purple trace in Fig. 5) decays the slowest. The case with $t_{lim} = 100$ (yellow trace) decays at a faster rate and exhibits a change in the rate of decay at times greater than t_{lim} . The case with the shortest memory persistence (orange trace) decays at the fastest rate but is still slower than the “No memory” case.

The spatial profiles at the end of the numerical calculations, $t = t_{up} = 200$, are shown in Fig. 6. The rate of profile spreading is determined by parameter a and the value of t_{lim} . The only profile to contact the system boundaries is the “No memory” case; all profiles of the cases with memory are contained within the system.

C. Mixed nonlocal transport

Figure 7 shows an example of transport when both subdiffusion (blue trace) and superdiffusion (yellow trace)

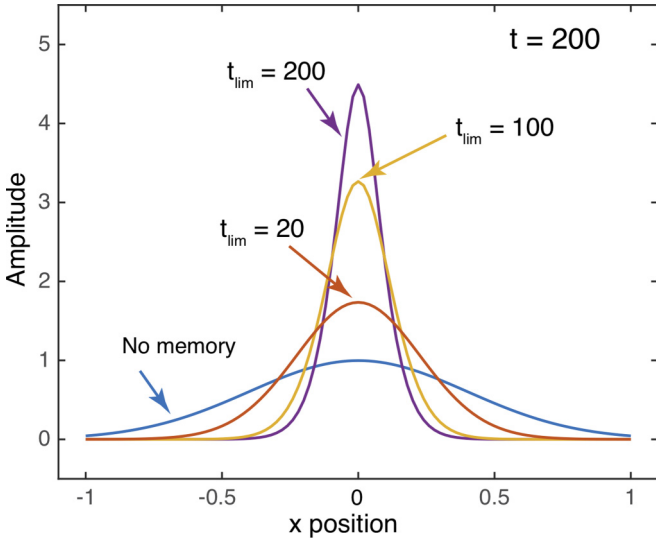


FIG. 6. The spatial profiles at scaled time $t = 200$ for the four cases shown in Fig. 5. For the three memory cases shown, none of the profiles reach the system boundaries, while the profile corresponding to standard diffusion (blue trace) reaches the system boundaries.

are present. For comparison to previous results, the sub-diffusive case with the slowest rate of profile decay [$a = 0.9, t_{lim} = 200$] is combined with the superdiffusive case with the fastest rate of decay [$a = 1, \alpha = 1.5$] to give a case [$a = 0.9, t_{lim} = 200, \alpha = 1.5$]. The combined case (orange trace) has a decay rate intermediate between the subdiffusive and superdiffusive cases. Figure 7(a) shows the natural logarithm of the profile amplitude at $x = 0$ versus the natural logarithm of time for all three cases. Figure 7(b) compares the spatial profiles for the three cases at the last time point in the calculation, $t = 200$. It is apparent that subdiffusive processes are very effective at slowing the rate of decay and spatial spreading of the temperature profile.

V. ANOMALOUS TRANSPORT WAVES

For a system whose dynamics is governed by a transport equation, such as the jumping particle equation, temporal oscillations in the source propagate but not as plane waves. That is, the trajectories of constant phase of the spatial and temporal oscillations are not proportional to $x = \omega/k t$. As an example, consider the diffusion equation with constant diffusion coefficient $D_c = 1, \partial T/\partial t = \partial^2 T/\partial x^2$. A solution proportional to $\exp(-i(\omega t - kx))$ results in the phase relation $i\omega = k^2$. Constant phase trajectories for the diffusion equation are parabolic rather than linear, and the amplitude experiences strong spatial attenuation. It is instructive to investigate the behavior of “wave” propagation in systems with anomalous transport [19]. Waves are generated by starting with steady-state conditions and sinusoidally oscillating the source amplitude by a small amount. Details of applying the iteration method to obtain steady-state profiles are given in [8]. In cases with superdiffusion and subdiffusion, constant phase trajectories in a system with an oscillating source can be rather complicated, but all such cases are lumped together in this study under the heading “anomalous transport (AT) waves.” Calculations of AT waves

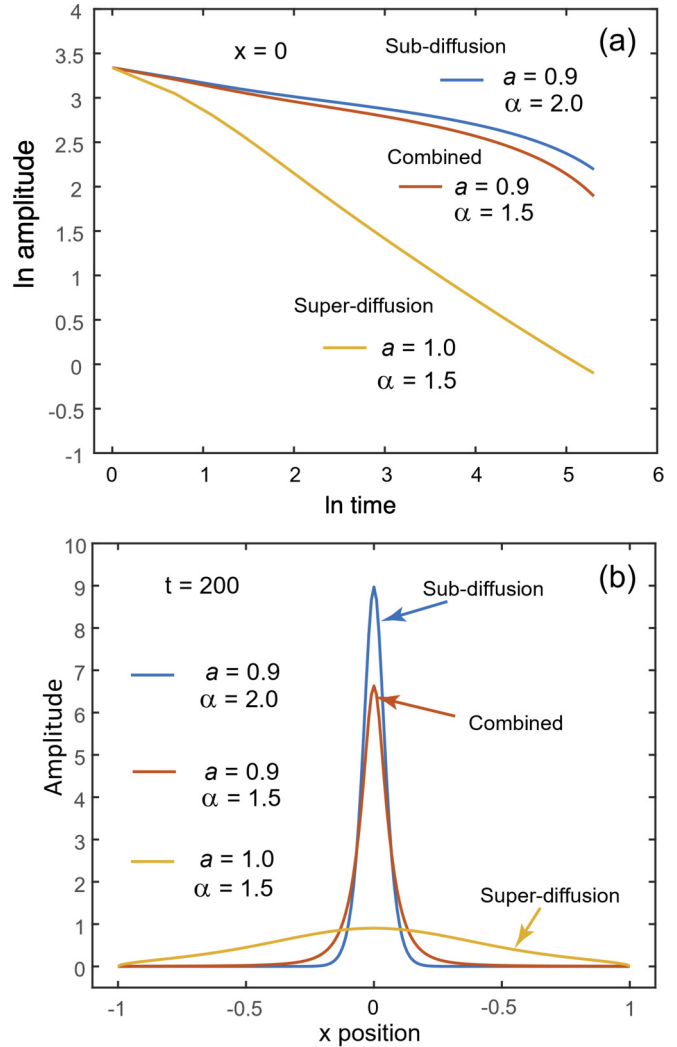


FIG. 7. Combining the subdiffusive process [$a = 0.9, t_{lim} = 200, \alpha = 2$] (blue trace) with the superdiffusive process [$a = 1, \alpha = 1.5$] (yellow trace) results in an intermediate behavior [$a = 0.9, t_{lim} = 200, \alpha = 1.5$] (orange trace). (a) The natural logarithm of the amplitude at $x = 0$ vs the natural logarithm of time for the three cases. (b) The spatial profiles at scaled time $t = 200$ for the three cases.

in 1D are performed using the 1D version of Eq. (10) given by Eq. (15).

A. AT waves in 1D

The temporal and spatial behavior of 1D oscillations in the presence of superdiffusion and no memory (i.e., $a = 1$) is calculated for three values of α : $\alpha = 2, 1.8,$ and 1.5 . AT waves are excited in a system in steady state by introducing a small sinusoidal oscillation of the source. The AT wave patterns are found by taking the difference between the system with the oscillating source and the steady-state system.

Steady-state profiles for the three values of α are shown in Fig. 8(a) along with the steady-state source. AT waves are generated by modulating the source amplitude for a limited time interval. The source amplitude is modulated by 5% for seven cycles, as shown in Fig. 8(b).

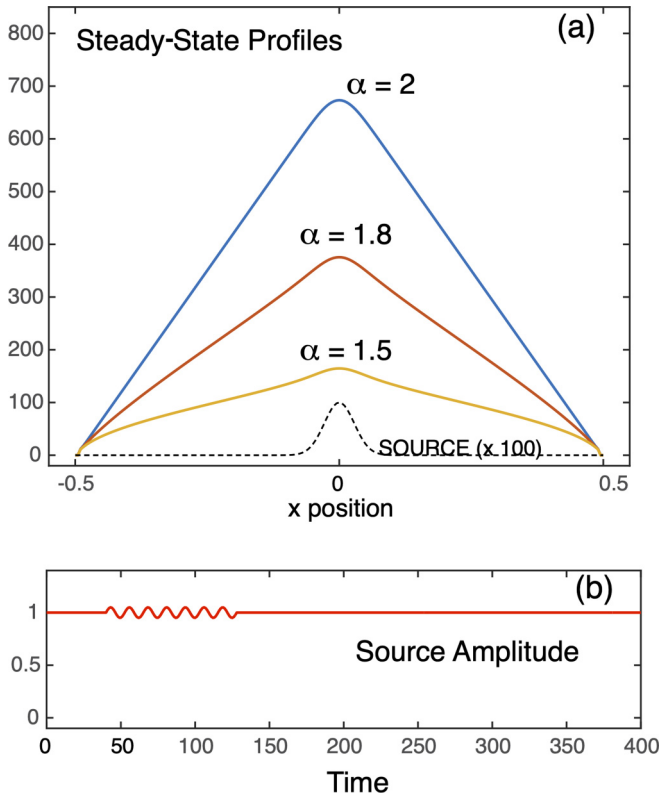


FIG. 8. (a) Steady-state profiles for three values of α and the corresponding steady-state source (dashed black line). The steady-state source is multiplied by a factor of 100 for clarity. (b) The amplitude of the modulated source.

Figure 9 shows contours of the difference between the modulated profile and the steady-state profile for each case. The time shown covers the interval after the source modulation ceases. “Waves” are launched by the modulated source. The “waves” are not plane waves, but rather profile structures that propagate and thus resemble waves. Shown in each panel of Fig. 9 are the locations in time and space of the wave crests and wave phases. These two quantities can behave differently. The wave crest is the location of the maximum of the spatial profile at a fixed time. Note from Fig. 9 that the location of a wave crest is at the maximum temporal extent of a given contour. In contrast, the wave phase is the location of the maximum of the temporal profile at a fixed position. Figure 9 indicates that the wave phase location coincides with the largest spatial extent of a given contour.

Figure 10(a) shows the paths of both the AT wave crests and wave phases as functions of space and time. The solid curves are the same as those shown in Fig. 9, but in this figure each value of α is color-coded. The wave crest paths show the time and space locations of the spatial maximum of the difference profile for positive values of x -position and for scaled times between 130 and 400. The spatial profiles of the AT waves are shown in Fig. 10(b) for all α values at time $t = 230$. The vertical yellow arrow shows the relation of the wave crest path to the spatial profile at $t = 230$ for $\alpha = 1.5$. The wave phase paths show the time and space locations of the temporal maximum for negative values of

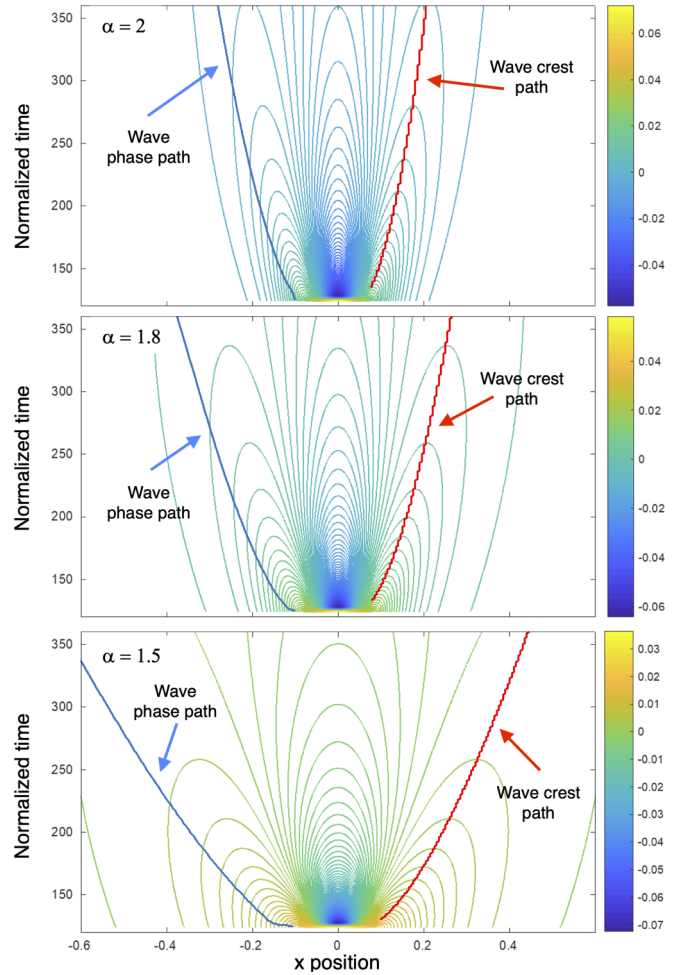


FIG. 9. Color contours of the difference between profiles in the modulated system and the steady-state system are shown for three values of α . Also shown are the trajectories in space and time of the wave crests and wave phases for each value of α (see also Fig. 10). These waves correspond to the superdiffusive regime without memory effects ($a = 1$). The amplitude color bar for each panel is on the right.

x -position and for times between 130 and 400. The maximum in time of the AT waves is related to the maximum in time of the source modulation. The dashed black lines are fits to each wave crest and wave phase path. The fits have the form $x_{fit}(t) = a_f + b_f t^{1/\alpha}$. The behavior of the wave crest paths is the same as the self-similarity variable of the Green’s function for 2D nonlocal transport as described by Kullberg *et al.* [20]. Both the wave phases and wave crests follow the space-time behavior of the self-similarity variable, but the fitting parameters (a_f, b_f) differ for each case.

A method for studying superdiffusive transport in azimuthally symmetric 2D systems was developed by Kullberg *et al.* [20]. In contrast to the techniques used in the present study, their method is based on a fractional Laplacian operator, and the temporal dynamics represented by a first derivative in time, i.e., without memory effects. That previous study identifies a self-similarity variable, denoted as λ , associated with the propagator function (Green’s function) that describes the radial propagation of δ -function pulses. The

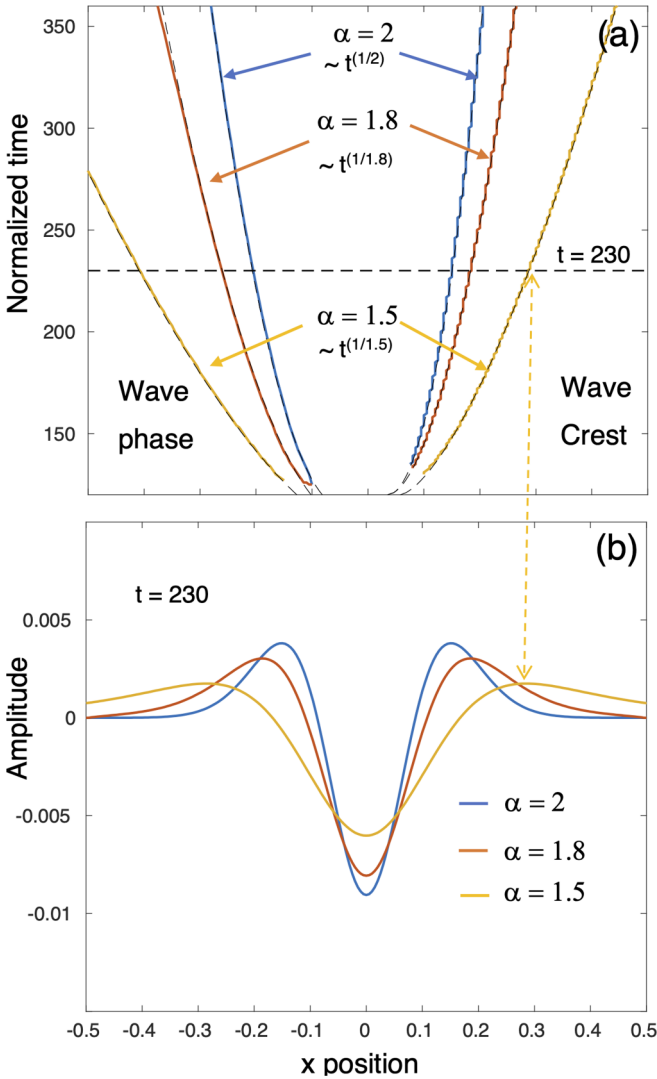


FIG. 10. (a) The paths of the wave crests for the three values of α are shown as functions of positive x -position and time. The paths of the wave phase are shown for the three values of α as functions of negative x -position and time. The solid curves are data extracted from the contour plots shown in Fig. 9. The dashed lines (barely visible due to overlap) are proportional to $t^{1/\alpha}$. (b) Spatial profiles of AT waves launched by the modulated source are shown for three values of α without memory effects ($a = 1$). The vertical yellow arrow relates the wave crest to the wave crest path at $t = 230$.

self-similarity variable is (Eq. 42 of [20]),

$$\lambda = \frac{\bar{r} - \bar{r}'}{(\bar{\chi}_\alpha \bar{t})^{1/\alpha}} = \frac{r - r'}{\gamma t^{1/\alpha}}. \quad (17)$$

In Eq. (17), barred variables are in physical units and unbarred variables are normalized. The second form of the self-similarity variable in Eq. (17) arises from defining the transport coefficient associated with the jumping particle model as $\bar{\chi}_\alpha = \bar{\gamma}^\alpha / \bar{\tau}$, where $\gamma = \bar{\gamma}/L$ is the characteristic spatial scale of the Lévy jump distribution, and $\bar{\tau}$ is the characteristic waiting time associated with the waiting-time distribution. In 1D the self-similarity variable in Eq. (17) has the same form as the function used to fit the wave crest paths

shown in Fig. 10(a), $x_{\text{fit}}(t) = a_f + b_f t^{1/\alpha}$ with $a_f = x'$ and $b_f = \lambda \gamma$.

The study of AT waves when subdiffusive processes are present also uses the method of modulating the steady-state source amplitude by 5% for a brief time interval. The difference is that the time vector is 201 points in length, $t_{\text{up}} = 200$, and the source oscillations are present for two cycles over the range $6 \leq t \leq 31$ with an oscillation period equal to 12.5. An illustration of the source modulation is shown in Fig. 12. Only the behavior of wave crest paths is shown for the subdiffusive case.

Figure 11(a) shows contours of AT wave amplitudes for a system with $\alpha = 2$, $a = 0.9$, and $t_{\text{lim}} = 20$. The display is limited to positive x -values in the range $0 \leq x \leq 0.5$, and to the time interval after the source oscillations are absent, $40 \leq t \leq 200$. The space-time path of the AT wave crest is indicated by the blue trace. In this case, AT waves spread out at a rate slower than the rate for standard diffusion ($a = 1$). The space-time path of the crest is proportional to $t^{0.45}$ (indicated by the dashed black trace) in contrast to the $t^{0.5}$ dependence in the no-memory case ($a = 1$). With a Mittag-Leffler waiting-time PDF, del Castillo–Negrete [18] defines a similarity variable associated with the Green’s function, $\eta = \bar{x}(\bar{\chi}_{\alpha a} \bar{t})^{-a/\alpha} = \frac{x}{\gamma} t^{-a/\alpha}$ with $\bar{\chi}_{\alpha a} = \bar{\gamma}^\alpha / \bar{\tau}$. The wave crest path shown in Fig. 11(a) follows a space-time path proportional to the similarity variable, $x \sim \eta t^{a/\alpha} \sim t^{0.9/2} = t^{0.45}$.

Figure 11(b) illustrates AT wave propagation for the case with $\alpha = 2$, $a = 0.9$, and $t_{\text{lim}} = 100$. Two very distinct propagation regions are evident. At times shorter than the memory persistence ($t < 100$), AT waves appear to propagate toward the center of the system. At longer times, AT waves propagate outwards away from the source region. An interesting phenomenon, evident in Fig. 11(b), is an “echo” of the modulated source appearing in the system response in the time range, $105 < t < 135$. The inward propagation phenomenon and the source echo arise because of the change in the waiting time PDF describing this system. The slowly decaying tail of the modified Mittag-Leffler PDF transitions to an exponential decay after times exceeding the memory persistence time (refer to Fig. 4). The slowly decaying portion of the PDF leads to a persistence of the source profile in the wave profile for times up to t_{lim} . The persistence of the source leads to the appearance of inward propagation because the source profile dominates the wave profile. The slowly decaying portion of the PDF also tends to smooth out the temporal oscillations in the modulated source. When the PDF transitions to exponential decay, the smoothing effect is absent and the source reappears, at low amplitude, in the system response (the “echo”). The “echo” phenomenon occurs because the transition from a model system with memory ($a < 1$) to one with no memory ($a = 1$) is abrupt. Such an abrupt transition is probably “unphysical” and may not occur in real systems.

Figure 11(c) presents a case with a persistent memory, that is, a case in which the persistence time is equal to or longer than the time vector used in numerical calculations. For this case, $\alpha = 2$, $a = 0.9$, and $t_{\text{lim}} = 200$. With persistent memory, AT waves appear to propagate inward rather than outward because the source profile (located in the system center)

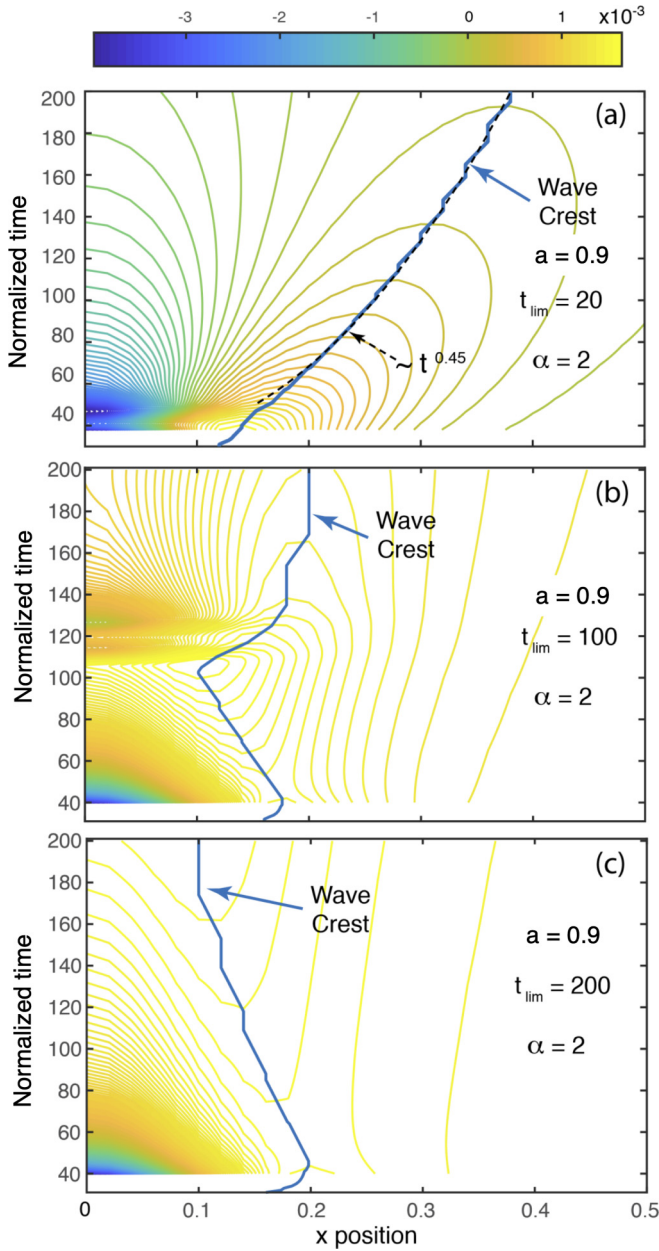


FIG. 11. (a) Contours illustrating AT wave propagation for a case with limited memory, $t_{lim} = 20$. As expected for a subdiffusive process, the wave crests spread away from the center at a rate proportional to $t^{0.45}$ as indicated by the dashed black trace. (b) Contours for the case in which memory lasts for 100 waiting times. While the memory persists, the AT wave appears to propagate toward the center of the system. At times later than the persistence time, wave crests spread away from the center. (c) Contours illustrating AT wave propagation in the case of persistent memory. With persistent memory, AT waves appear to propagate inward because of the persistence of the source profile at all times. A line cut of the temporal behavior at $x = 0$ for these three cases is shown in Fig. 12.

becomes increasingly dominant as the wave profile decays with time.

Figure 12 shows the temporal behavior of AT waves at the center of the system. Figure 12(a) is an overview that illustrates the response of each individual system shown in

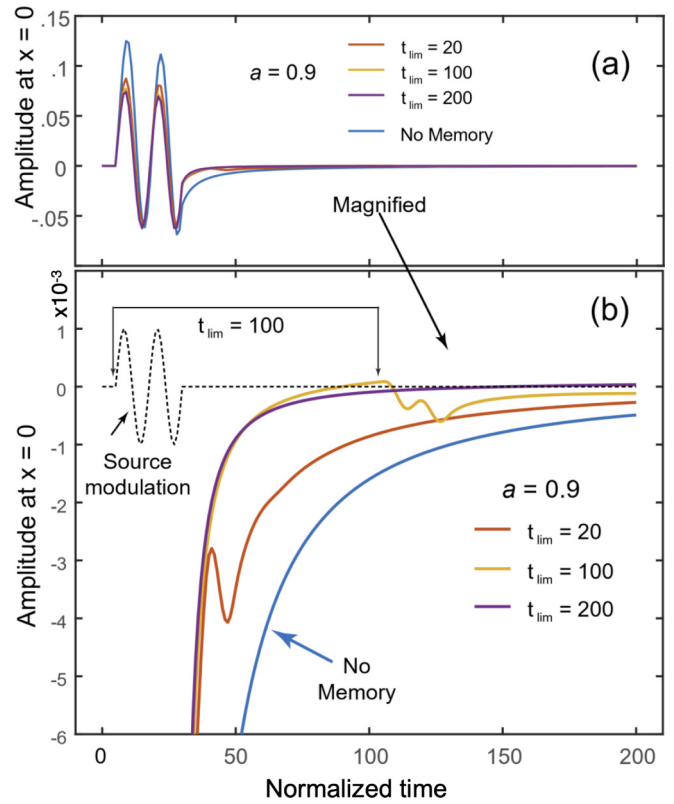


FIG. 12. The temporal behavior of AT waves at the center of the system. Panel (a) shows the response to the source modulation. Panel (b) presents a magnified view illustrating the delayed response, or echo, to the source in the cases with limited memory persistence.

Fig. 11 to the modulated source. For comparison, the standard diffusion case with $\alpha = 2$ and $a = 1$ is also shown and labeled as “No memory.” The largest amplitude response occurs for the system with “No memory.” Figure 12(b) is a magnification of the curves in panel (a) that elucidates the source “echo” response. The yellow trace in Fig. 12(b) is for the system with memory persistence equal to 100 waiting times. The dashed black trace shows the temporal behavior of the source modulation. Source oscillations reappear in the system response one persistence time ($t_{lim} = 100$) after the source oscillations begin as indicated by the arrows in Fig. 12(b). Source oscillations also reappear in the system with shorter memory persistence (orange trace, $t_{lim} = 20$) but are not as evident in the contour plot shown in Fig. 11(a). No source echo is present in either the system with persistent memory (purple trace) or the system with “No memory” (blue trace).

Figure 13(a) presents a summary view of the space-time paths for AT wave crests shown in Fig. 11. The “No memory” case is also included for comparison. All wave crest paths for the cases with memory indicate that AT waves spread much slower away from the source as compared to the standard diffusion case. Figure 13(b) shows the spatial profiles at $t = 200$. The profile for the “No memory” case has reached the system walls, while all the other profiles have yet to reach the system boundaries. The profiles for the systems with limited memory persistence (orange and yellow traces) have shapes like that of the “No memory” case (blue trace), a negative minimum in

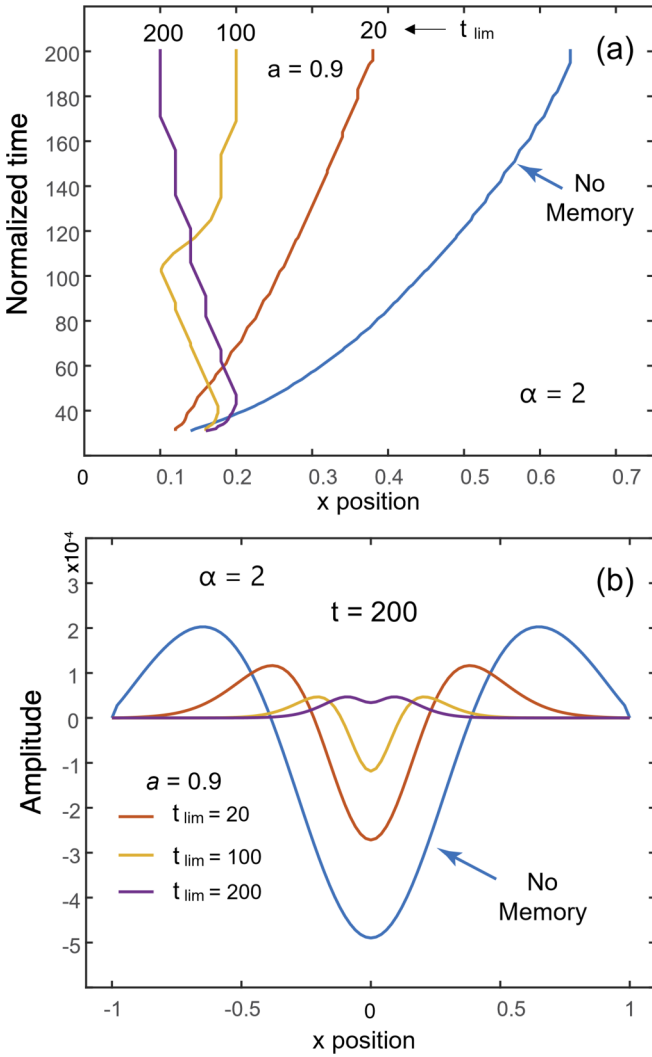


FIG. 13. (a) The space-time wave crest paths from Fig. 11 are plotted together with the path for standard diffusion (“No memory”) for easy comparison. (b) The spatial profiles of the waves at $t = 200$. The profile for the case with $a = 0.9$ and $t_{lim} = 200$ is positive everywhere due to the persistence of the source profile.

the center of the system flanked by two positive maxima. The influence of the source profile for these two cases is absent at this late time. The mean spatial value of these two profiles is zero. In contrast, the profile for the system with persistent memory is positive everywhere because of the influence of the source.

B. AT waves in 2D

Figure 14 shows contours of AT wave propagation in a 2D system with azimuthal symmetry and $\alpha = 1.7$ and $a = 1$. Two values of the jump distribution width are used. One system has $\bar{\gamma}/\bar{L} = \gamma = 0.005$ and the other has a jump width twice as large, $\gamma = 0.01$. The effective transport coefficient is proportional to γ^α so that the system with a jump distribution width two times larger has a transport coefficient 3.25 times larger. The spatial calculation grid in the 2D system has grid spacing $h = 0.01$ and the calculation time is half the size of

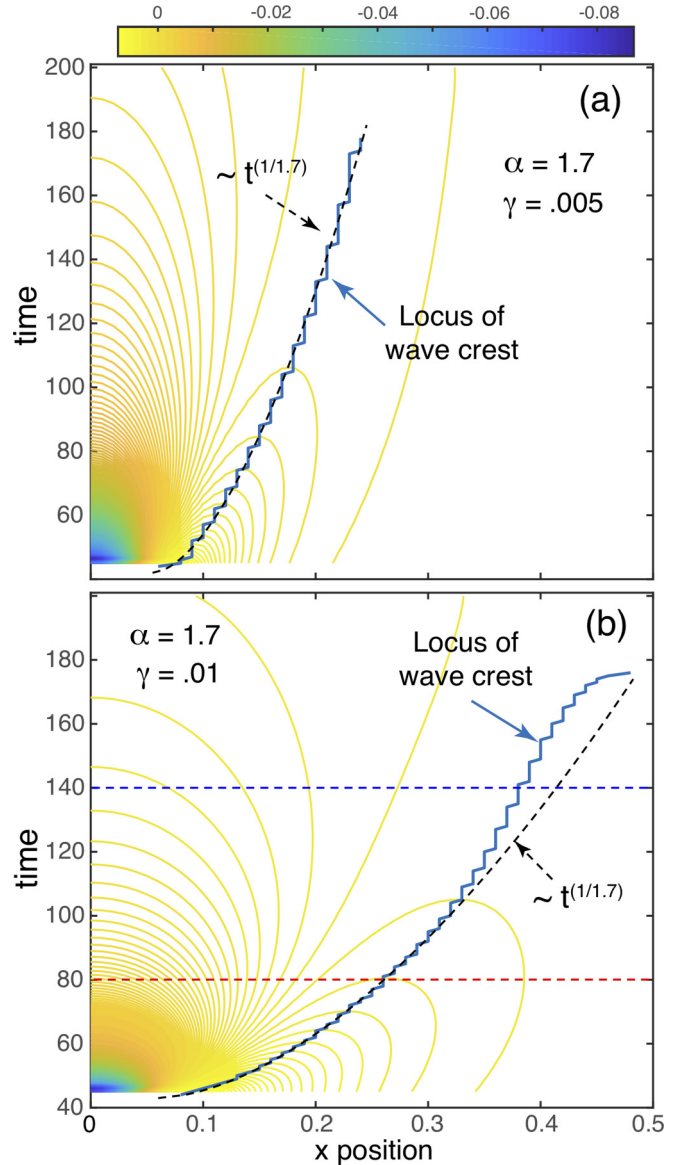


FIG. 14. Contours of AT wave propagation along the radial direction in an azimuthally symmetric 2D system. (a) System with a small jump distribution width, $\gamma = 0.005$. (b) System with a larger jump distribution width, $\gamma = 0.01$.

that in the 1D calculations. As indicated by Eq. (17), propagation of AT waves is expected to follow a curve proportional to $t^{1/\alpha}$, or in this case with $\alpha = 1.7$, $t^{0.5882}$. The dashed black lines in Fig. 14 are the expected paths of AT wave propagation. The actual locations of the AT wave crests are indicated by the solid blue traces. The jagged appearance of the actual wave crest paths is due to the limited spatial resolution of the computation grid. The two curves agree quite well for the smaller value of γ , $\gamma = 0.005$, but the two curves diverge at late times for the larger γ value. The propagation of AT waves in the 2D system with $\gamma = 0.01$ shows the effects of finite system size. The system is “small” for the larger value of transport coefficient. AT wave propagation is changed as the waves approach the system boundary. At early times, the wave crest trajectory [blue trace in Fig. 14(b)] follows expected behavior.

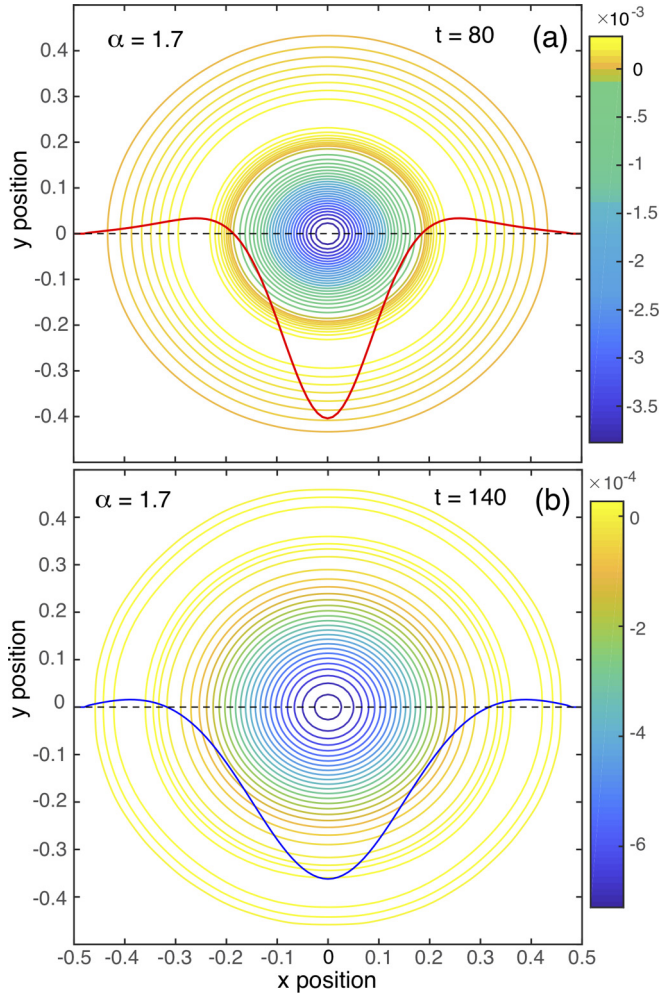


FIG. 15. (a) Contours of AT wave amplitude with $\gamma = 0.01$ at time $t = 80$ [red dashed line in Fig. 14(b)]. (b) Contours of AT wave amplitude with $\gamma = 0.01$ at time $t = 140$ [blue dashed line in Fig. 14(b)]. Solid curves are values along the dashed lines.

At intermediate times, the wave slows as it approaches the system boundary. At very late times, the maximum value of the wave occurs at the boundary because, at late times, the wave has negative values over the entire system.

Contours of wave amplitude together with spatial profiles taken along a diameter are shown in Fig. 15. Two times are chosen for display, as indicated by the dashed lines at constant time in Fig. 14(b). The first time at $t = 80$ (red dashed line) is when the wave is not interacting with the boundary, and the second time at $t = 140$ (blue dashed line) is when the wave is interacting with the boundary.

The time-dependent jumping particle model is capable of handling nonuniform 2D systems. As a demonstration, a model system representing a fictional magnetic confinement device is chosen to study the propagation of AT waves. Figure 16 displays the geometry of the magnetic surfaces of the model system. The fictional scenario chosen mimics a transport device by having very strong transport along magnetic surfaces as opposed to transport across magnetic surfaces. The spatial jump distributions that model this transport scenario are described by Eq. (11) of Ref. [21]. The width of the

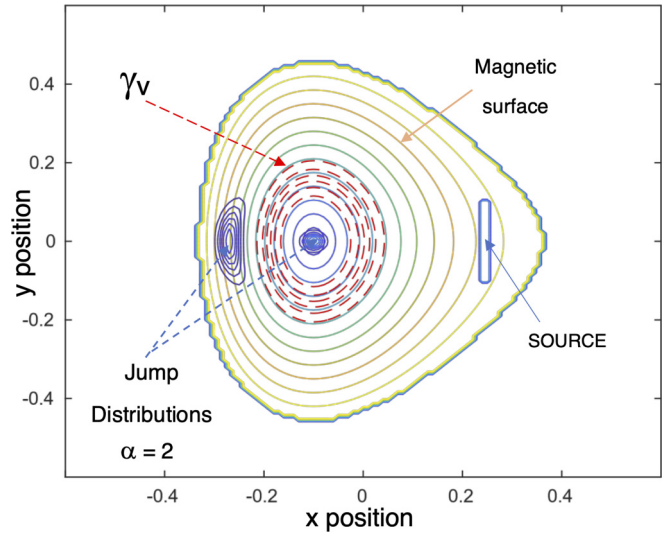


FIG. 16. Magnetic surfaces that mimic a magnetic confinement device are used to provide a 2D asymmetric geometry. The jump distribution width in the direction along magnetic surfaces (γ_v) varies with position as indicated by the dashed, red contours. The jump distribution width across magnetic surfaces is uniform. Contours (as indicated) show the spatial shape of two jump distributions with $\alpha = 2$.

jump distribution along magnetic surfaces [6], labeled γ_v , is one grid spacing in the center of the magnetic surfaces and increases to four grid spacings in regions near the boundary, as indicated by the red, dashed contour lines in Fig. 16. The jump distribution width across magnetic surfaces, γ_u , is unity everywhere. Two values of the α parameter are chosen to study wave propagation: $\alpha = 2$ and 1.5. Contours of the jump probability distribution with $\alpha = 2$ and these choices of γ_u and γ_v are shown at two locations in Fig. 16. One example is located at the center of the magnetic surfaces where $\gamma_v = \gamma_u = 1$ and is isotropic. The other is in the outer regions where $\gamma_v = 4$, $\gamma_u = 1$ and it is strongly asymmetric.

Waves are launched by modulating a source located as shown in Fig. 16. The steady-state temperature profile associated with the source and magnetic surface geometry is computed. Waves are launched by modulating the source amplitude by 5% for two cycles with a period of 12.5 normalized time units. The modulation occurs over the normalized time interval $6 \leq t \leq 31$. Wave behavior is studied by taking the difference between the modulated source profile and the steady-state profile. Figure 17 shows the waves launched by the oscillating source for the two α values at $t = 54$. Contours of spatial amplitude are shown, rather than a time-space plot, as they present a clearer picture of the difference between the two cases. For the time shown, the nonlocal waves with $\alpha = 1.5$ (dashed contours) have reached the center of the magnetic surfaces, while the local, $\alpha = 2$, waves (solid contours) have not. Both wave patterns exhibit the effects of the strong asymmetry in the jump distributions, but the nonlocal case propagates across and along magnetic surfaces at a faster rate than the local case even though the jump distribution widths are the same for the two cases. The transport coefficient is proportional to $(\bar{\gamma}/\bar{L})^\alpha$, and since $\bar{\gamma}/\bar{L} < 1$ the $\alpha = 1.5$ case has a larger transport coefficient than the $\alpha = 2$ case.

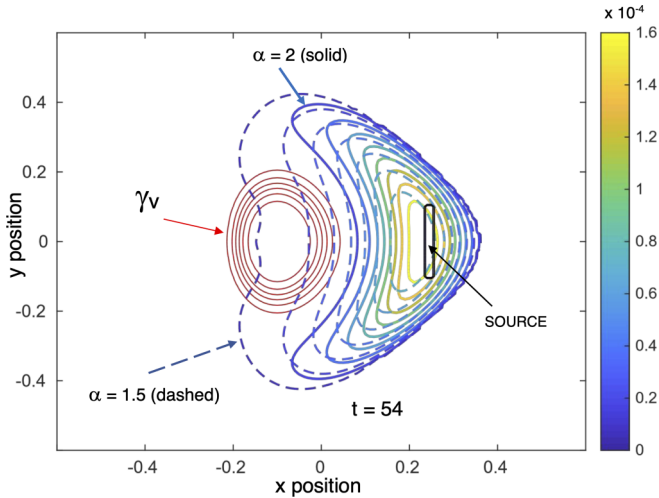


FIG. 17. Contours of wave amplitude for the two α values are shown at $t = 54$. Solid contours show the wave pattern for $\alpha = 2$ and dashed contours for $\alpha = 1.5$. The change in γ_v , the jump distribution width along magnetic surfaces, from 1 in the center to 4 on the periphery, is indicated by the red contour lines.

VI. DISCUSSION AND CONCLUSIONS

This study uses the master equation of the “jumping particle” model introduced by Montroll and Weiss [9] to model complex nonlocal transport problems that arise in bounded systems whose zero-order parameters vary with position. The key elements of the model are a probability distribution for the size of particle jumps in space and a probability distribution for the length of time a particle “waits” before jumping. The probability distribution functions used to represent spatial dynamics are Lévy α -stable distributions characterized by two parameters: the distribution width, γ , and the distribution order, α . The distribution width of the spatial PDF, γ , is referred to as “the step size.” Lévy distributions are characterized by “long tails” and are associated with the dynamics of superdiffusion. The waiting-time probability distribution is taken to be a modified form of the Mittag-Leffler function characterized by the parameters a and t_{lim} . The modified version of the function can represent a dynamic process with no memory by setting $a = 1$, in which case t_{lim} is not relevant. Processes with memory of limited persistence are represented by choosing $a < 1$ and a value of t_{lim} less than the length of the computation time vector. The value of t_{lim} then determines the length of time the memory effect persists.

It is demonstrated that the jumping particle model equation with parameter values $a = 1$ and $\alpha = 2$ contains spatial derivatives higher than second order, giving rise to a transient initial response that decays rapidly with time. The jumping particle model with these parameter values represents the standard diffusion equation at long times. The Lévy α -stable jumping particle probability distributions with $1 \leq \alpha < 2$ lead to nonlocal spatial transport that is superdiffusive, that is, faster than Fick’s law diffusion. The modified Mittag-Leffler waiting time distribution with $a < 1$ describes transport processes with memory. Memory effects lead to subdiffusive transport, that is, transport at rates slower than standard diffusion. Limited memory persistence results in transport that is

faster than transport with persistent memory but still slower than transport without memory. It is found that memory is very effective at suppressing the profile spreading effects of nonlocality.

The utility of the model in solving time-dependent problems is illustrated by investigating the propagation of waves in situations when anomalous transport processes are present. These so-called anomalous transport (AT) waves are investigated in 1D and 2D systems by starting with a steady-state system and sinusoidally modulating the amplitude of the source. Both the wave maximum and the wave phase of anomalous transport waves in 1D with nonlocal jump distributions and no memory propagate along space-time paths with functional dependence $x \sim t^{1/\alpha}$. Spatial nonlocality ($\alpha < 2$) leads to waves that spread faster than normal diffusion waves ($\alpha = 2$). In the situation with memory of limited persistence ($a < 1$) and local diffusion ($\alpha = 2$), the space-time paths associated with wave features have the functional form $x \sim t^{a/\alpha}$ for times longer than the memory persistence time. For times less than the memory persistence time, wave profiles are influenced by the persistence of the source profile.

The propagation of AT waves was studied in an azimuthally symmetric 2D system with no memory and nonlocal spatial transport ($\alpha = 1.7$). With a 101×101 calculation grid and a step size of half a grid spacing ($\gamma = 0.005$), the wave crests follow the expected space-time path, $r \sim t^{1/1.7}$. For a step size twice as large, wave propagation is affected by the system boundaries, illustrating that the concept of system “size” is dependent upon the magnitude of the transport coefficient.

AT wave propagation in a geometry that mimics a magnetic confinement device was studied as an application of the time-dependent jumping particle model in a nonuniform 2D system. Two transport scenarios were investigated, one with $\alpha = 2$ (local, Fick’s law transport) and the other with nonlocal transport with $\alpha = 1.5$. Both transport scenarios have the same jump sizes as a function of position. Jump sizes are constant and equal to one grid spacing across magnetic surfaces. The jump size in the direction along magnetic surfaces is one grid spacing in the center of the magnetic surfaces, and it increases to four grid spacings towards the outer regions of the magnetic surfaces. It is shown that the propagation speed of AT waves is asymmetric, with waves spreading fastest along the magnetic surfaces in concert with the transport coefficient. Wave propagation is faster for the nonlocal case as compared to the local case.

The advantage of the method over the explicit use of fractional derivatives is that it can handle irregularly shaped boundaries and spatial variations in the parameters. Since the fractional derivative approach results from an asymptotic approximation to the underlying CRTW jumping particle model, it is, in a certain sense, automatically included in the integral formulation presented here. The scaling properties extracted from the fractional derivative formulation are reproduced by the numerical solutions of the time-integral, iterative method.

In the model, the number of free parameters is, at a minimum, α , γ , and the shape of the boundary. There could be more parameters as when magnetic coordinates are used, and γ varies along and across the field. Also, spatial variations in any or all of the parameters can occur. Using the maximum

size of the system to scale spatial variables is a convenience but not a necessity. Any physically meaningful length could in principle be used for scaling. A rectangular grid was used for simplicity in the results shown, but the method can also handle irregular calculation grids. Also, the method is easily extended to 3D, but, as is natural, the computational resources needed for its implementation become quite demanding.

Although a magnetic confinement system was used to highlight the capabilities of the methodology (Figs. 16 and 17), the time-dependent iteration technique should be useful for describing general systems that exhibit anomalous transport. The method can handle subdiffusive and superdiffusive systems in which boundaries play an important role. Some examples of possible applications include anomalous transport in living cells [23,24], in crowded polymer solutions [25] and crowded lipid bilayers [26], flows in porous media [27] and in nanofluids between parallel plates [28], heat fluctuations in carbon lattices [29], and models of societal events [30,31].

APPENDIX

It is instructive to determine the extent to which the jumping particle model with the parameter set $[\alpha = 2, a = 1]$ represents the process of standard diffusion (Fick's law). When the parameter α equals 2 ($\alpha = 2$), the spatial jump distribution is a Lévy-stable distribution with $\alpha = 2$ and jump step size γ and is equivalent to a Gaussian distribution with $\sqrt{2} \sigma = \gamma$. The diffusion coefficient associated with this jump distribution is $D_c = \gamma^2$. When the Mittag-Leffler parameter is unity ($a = 1$), the waiting-time distribution is the Poisson distribution, which is proportional to the exponential function, $\exp(-t)$. The relation of the jumping particle model to standard diffusion is investigated by comparing numerical solutions in 1D to the analytic 1D diffusion problem given in Eq. (16). For comparing the jumping particle model to standard diffusion, it is useful to have a 1D version of the time-dependent jumping particle model. The 1D version of Eq. (10) with a Poisson waiting-time distribution is

$$T(t, x) = \int_0^t ds e^{-(t-s)} \int_0^1 dx' \eta'(p(x'), x - x') T(s, x') + T_0(x)e^{-t} + S(t, x). \quad (\text{A1a})$$

An equation equivalent to Eq. (A1a) is

$$\int_0^1 dx' \eta'(p(x'), x - x') T(t, x') = \frac{\partial T(t, x)}{\partial t} + T(t, x) + S_1, \quad (\text{A1b})$$

$$S_1(t, x) = S(0, x)e^{-t} + e^{-t} \frac{\partial [e^t S(t, x)]}{\partial t}.$$

In addition, results can also be compared to the 1D transport matrix model described by Maggs and Morales [22]. The time-dependent transport matrix model equation is

$$T^{m+1} = \left[\tilde{a}I + \frac{M_w^{-1}}{\Delta t} \right]^{-1} \left\{ \left[-(1 - \tilde{a})I + \frac{M_w^{-1}}{\Delta t} \right] T^m + M_w^{-1} \tilde{S}^m \right\}. \quad (\text{A2})$$

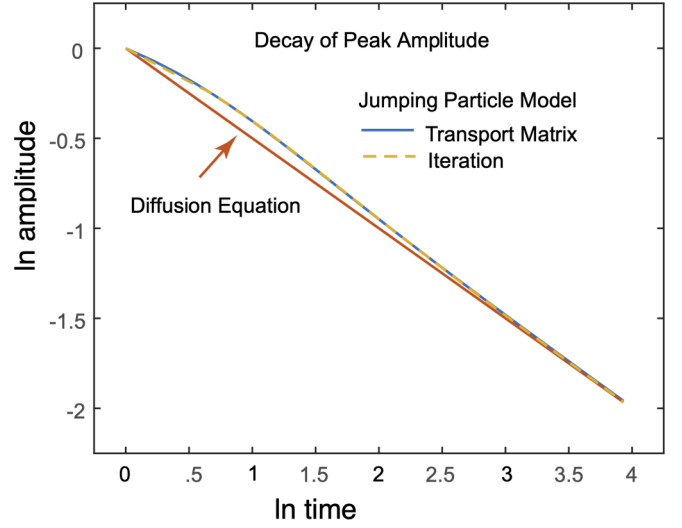


FIG. 18. The temporal decay of the natural logarithm of the profile amplitude at $x = 0$ is compared for two numerical solutions of the jumping particle model and the diffusion equation.

The term T^m denotes the solution vector at time $t = m\Delta t$, $T^m = T(m, i)$, and the source S -tilde is $\tilde{S}^m = \tilde{a}S^{m+1} + (1 - \tilde{a})S^m$ with $\tilde{a} = (3 - \alpha)/2$. The identity matrix is denoted by I , and M_w^{-1} is the inverse of the transport matrix, M_w .

In 1D, steady-state solutions of the jumping particle model agree closely with analytic solutions of the diffusion equation, except near the boundaries because of the boundary interface used in the jumping particle model. The $\alpha = 2$ jump distribution reasonably represents the standard Fick's law diffusion in the steady-state case. The temporal problem is a different matter. To test the temporal behavior, the analytic solution shown in Eq. (16) is compared to the results of iterating the 1D time-dependent jumping particle model, Eq. (A1a). Solutions to Eq. (A1a) are obtained by starting with the analytic profile, T_A , given in Eq. (16), evaluated at $t = 1$, as an initial profile. That is, the initial profile of the iterated solution is $T_A(1, x) = \exp(-x^2/4D_c)/2\sqrt{\pi D_c}$. This initial profile is evolved forward in time using an iteration of the 1D jumping particle model [Eq. (A1a)] with Simpson's rule for the time integration. The iterated solution is compared to the analytic solution in Fig. 18. The comparison (yellow dashed line) shown in Fig. 18 is the natural logarithm of the amplitude of the profile at $x = 0$ versus the natural logarithm of time. Also shown in Fig. 18 is the solution (solid blue trace) obtained using the time-dependent transport matrix solutions obtained from Eq. (A2). The numerical solutions are compared to the analytic solution, shown by the solid orange line with a slope of -0.5 in this log-log plot. The two numerical solutions agree with each other but differ from the analytic solution.

The conclusion drawn from this exercise is that the time-dependent jumping particle model, as embodied by Eqs. (A1a) and (A2), does not represent the diffusion equation at early times. The difference between the jumping particle model and the diffusion equation can be elucidated by considering the spatial integration term that appears in the jumping particle model, $\int_0^1 dx' \eta'(p(x'), x - x') T(t, x')$. For

this exercise, consider a simplified version of this term, $\int_0^1 dx' \eta'(x-x')T(t, x')$, and change the integration variable to $x' \rightarrow x-x''$, so that the integral expression becomes

$$\int_0^1 dx' \eta'(x-x')T(t, x') \rightarrow \int_x^{x+1} dx'' \eta(x'')T(t, x-x''). \quad (\text{A3})$$

Expanding the expression $T(t, x-x'')$ in a Taylor series and using the expression in Eq. (A3) results in

$$\begin{aligned} & \int_0^1 dx' \eta'(x-x')T(t, x') \\ &= \int_x^{x+1} dx'' \eta'(x'')T(t, x-x'') \\ &= T(t, x) + \sum_{n=1}^{\infty} M^{(2n)} \frac{\partial^{2n} T(t, x)}{\partial x^{2n}}. \end{aligned} \quad (\text{A4})$$

In Eq. (A4), the first term on the right-hand side results because $\eta'(x)$ is a probability distribution and thus its integral is unity. In the summation over m , only even moments appear because the jump distributions are taken to be symmetric functions so that odd moments are zero. The even moments $M^{(2m)}$ are

$$\begin{aligned} M^{(2m)}(x) &= \int_x^{x+1} dx'' \frac{(x'')^{2m}}{2m!} \eta'(x'') \\ &\simeq \int_0^1 dx'' \frac{(x'')^{2m}}{2m!} \eta'(x'') = M^{(2m)}. \end{aligned} \quad (\text{A5})$$

The moments depend upon the variable x but, if x is not near the boundaries of the spatial interval so that the function

$\eta'(x'')$ is not truncated, the moments are constants as assumed in the last expression in Eq. (A5). The jumping particle model equation, Eq. (A1b), with the simplified spatial integral term, can be written as

$$\begin{aligned} \frac{\partial T(t, x)}{\partial t} &= \int_0^1 dx' \eta'(x-x')T(t, x') - T(t, x) \\ &\simeq \sum_{m=1}^{\infty} M^{(2m)} \frac{\partial^{2m} T(t, x)}{\partial x^{2m}}. \end{aligned} \quad (\text{A6})$$

If only the first moment term, $M^{(2)}$, is kept, the jumping particle model equation is the diffusion equation and $M^{(2)}$ is the diffusion coefficient. However, in addition to the first even moment, the jumping particle model equation contains all the higher, even, derivatives of the spatial profile. The $2m$ -moment term is proportional to $(\bar{\gamma}/\bar{L}_s)^{2m}$, where $\bar{\gamma}$ is the physical size of the average jump, and \bar{L}_s is the physical size of the gradient scale length of the temperature profile. The steady-state profiles associated with the jumping particle model contain these higher derivative terms, but they are negligible if, as is generally the case, $\bar{\gamma}/\bar{L}_s \ll 1$. In the steady-state case, the discrepancy in the profiles due to the boundary interface difference is many orders of magnitude larger than discrepancies associated with higher derivative terms. For the comparison of the jumping particle model to the analytic example given in Eq. (16), the profile scale length, $\bar{L}_s = 2\sqrt{D\bar{t}}$, increases with time while the average jump length, $\bar{\gamma}$, is constant. Thus, the ratio $\bar{\gamma}/\bar{L}_s \rightarrow 0$ as $t \rightarrow \infty$ so that the jumping particle model equation becomes the diffusion equation at long times, and the analytic solution agrees with the numerical solutions as indicated in Fig. 18.

-
- [1] R. Chen, S. Li, H.-P. Sun, Q. Liu, Y. Zhao, H. Z. Lu, and X. C. Xie, *Phys. Rev. B* **103**, L241409 (2021).
- [2] P. H. McGuinness, E. Zhakina, M. König, M. D. Bachmann, C. Putzke, P. J. W. Moll, S. Khim, and A. P. Mackenzie, *Proc. Natl. Acad. Sci. USA* **118**, e2113185118 (2021).
- [3] A. J. Wright, M. J. Erickson, D. Bromley, P. A. Crowell, C. Leighton, and L. O'Brien, *Phys. Rev. B* **104**, 014423 (2021).
- [4] H. Li and G. Ouyang, *Phys. Rev. B* **100**, 085410 (2019).
- [5] K. K. Ida, *Rev. Mod. Plasma Phys.* **6**, 2 (2022).
- [6] Y. Zhang, D. Zhou, M. Yin, H. Sun, W. Wei, S. Li, and C. Zheng, *Hydro. Proc.* **34**, 5104 (2020).
- [7] M. Vila, J. H. Garcia, A. W. Cummings, S. R. Power, C. W. Groth, X. Waintal, and S. Roche, *Phys. Rev. Lett.* **124**, 196602 (2020).
- [8] J. E. Maggs and G. J. Morales, *Phys. Rev. E* **99**, 013307 (2019).
- [9] E. Montroll and G. H. Weiss, *J. Math. Phys.* **6**, 167 (1965).
- [10] M. G. Mittag-Leffler, *C. R. Acad. Sci. Paris* **137**, 554 (1903).
- [11] R. Metzler, W. G. Glockle, and T. F. Nonnenmacher, *Physica A* **211**, 13 (1994).
- [12] P. Paradisi, R. Cesari, F. Mainardi, and F. Tampieri, *Physica A* **293**, 130 (2001).
- [13] D. del Castillo-Negrete, *Phys. Plasmas* **13**, 082308 (2006).
- [14] Y. Zhang, D. A. Benson, and D. M. Reeves, *Adv. Water Resources* **32**, 561 (2009).
- [15] I. Podlubny, *Fractional Differential Equations* (Academic, New York, 1999).
- [16] R. Hermann, *Fractional Calculus* (World Scientific, Singapore, 2011).
- [17] R. Gorenflo, J. Loutchko, and Yu. Luchko, *Fract. Calc. Appl. Anal.* **5**, 491 (2002).
- [18] D. del Castillo-Negrete, *Turbulent Transport in Fusion Plasmas: First ITER International Summer School*, edited by S. Benkadda, AIP Conf. Proc. No. 1013 (AIP, New York, 2008), p. 207.
- [19] R. Klages, G. Radons, and I. M. Sokolov, *Anomalous Transport: Foundations and Applications* (Wiley-VCH, Weinheim, 2008).
- [20] A. Kullberg, D. del Castillo-Negrete, G. J. Morales, and J. E. Maggs, *Phys. Rev. E* **87**, 052115 (2013).
- [21] J. E. Maggs and G. J. Morales, *Phys. Plasmas* **26**, 052505 (2019).
- [22] J. E. Maggs and G. J. Morales, *Phys. Rev. E* **94**, 053302 (2016).
- [23] M. Woringner, I. Izeddin, C. Favard, and H. Berry, *Front. Phys.* **8**, 134 (2020).
- [24] L. Bruno, V. Levi, M. Brunstein, and M. A. Desposito, *Phys. Rev. E* **80**, 011912 (2009).
- [25] D. Banks, C. Tressler, R. D. Peters, F. Hoffing, and C. Fradin, *Soft Matter* **12**, 4190 (2016).

- [26] J-H. Jeon, M. Javanainen, H. Martinez-Seara, R. Metzler, and I. Vattulainen, [Phys. Rev. X **6**, 021006 \(2016\)](#).
- [27] P. de Anna, T. Le Borgne, M. Dentz, A. M. Tartakovsky, D. Bolster, and P. Davy, [Phys. Rev. Lett. **110**, 184502 \(2013\)](#).
- [28] N. Ahmed, D. Vieru, C. Fetican, and N. A. Shah, [Phys. Fluids **30**, 052002 \(2018\)](#).
- [29] U. Ray and D. T. Limmer, [Phys. Rev. B **100**, 241409\(R\) \(2019\)](#).
- [30] M. ur Rahman, S. Ahmad, M. Arfan, A. Akgül, and F. Jarad, [Fractal Fract. **6**, 162 \(2022\)](#).
- [31] M. R. Lindstrom and A. L. Bertozzi, [Math. Models Methods Appl. Sci. **30**, 1863 \(2020\)](#).